A&A, 707, A179 (2026)
https://doi.org/10.1051/0004-6361/202557131

Astronomy & Astrophysics

Distributed accelerators in the jet of Centaurus A: Origin of the spectral hardening of very-high-energy gamma-rays

Y. S. Honda[1,⋆] and M. Honda[2]

[1] Kindai University Technical College, Nabari, Mie 518-0459, Japan
[2] Plasma Astrophysics Laboratory, Institute for Global Science, Mie, Japan

Received 6 September 2025 / Accepted 16 January 2026

ABSTRACT

We propose the synchrotron self-Compton (SSC) scenario coupled with a filamentary jet model to reproduce the very-high-energy γ-ray emissions from Cen A. With reference to self-similarity of knot-like features in the jet, we assumed a nonuniform magnetic field associated with current filaments of various transverse sizes. For energetic electron production, the diffusive shock acceleration at sites distributed over the kiloparsec-scale jet was considered. We show that the maximum Lorentz factor of the electron steadily exceeds 10^8 due to suppression of synchrotron loss of the electrons trapped in the weak magnetic field of the thin filaments, and an inhomogeneous SSC scenario in the inner jet can predominantly contribute to establishment of the pronounced hardening of γ-ray flux detected by the High Energy Stereoscopic System (H.E.S.S.). It is also suggested that the spectral contribution from diffuse regions of the outer jet potentially amounts to the observed Fermi fluxes.

Key words. acceleration of particles – radiation mechanisms: non-thermal – turbulence – galaxies: individual: Cen A – galaxies: jets

1. Introduction

The nearest radio galaxy, Centaurus A (NGC5128, at a distance of 3.8 Mpc from us; Harris et al. 2010) is known as a powerful γ-ray emitter and serves as a unique laboratory to study the radiative processes in the kiloparsec-scale jets and giant radio lobes. Intriguingly, the High Energy Stereoscopic System (H.E.S.S.) detected, in the γ-ray spectral hump, the unnatural hardening above 250 GeV (Aharonian et al. 2009; Abdalla et al. 2020), which exceeds the flux level extrapolated from the early Fermi-Large Area Telescope (LAT) data in the sub-GeV range (Abdo et al. 2010). The H.E.S.S. suggests the Lorentz factor of accelerated electrons reaches the order of 10^8. Although the single-zone synchrotron self-Compton (SSC) scenario (Chiaberge et al. 2001) can adequately reproduce the spectra of Cen A up to sub-GeV range detected by the Energetic Gamma Ray Experiment Telescope (EGRET) on Compton Gamma Ray Observatory (CGRO; Steinle et al. 1998), it is not accountable for the very high energy (VHE; 100 GeV–100 TeV) γ-ray fluxes detected by the H.E.S.S. (Abdalla et al. 2020). Abdo et al. (2010) constructed a multiband spectrum of Cen A core below ∼10 GeV using a single-zone SSC model, but required an alternative parameter set in such a way that would explain the early H.E.S.S. data beyond 100 GeV (Aharonian et al. 2009). Lenain et al. (2008) proposed a model of multiple blobs similar in size to and positioned at various angles with respect to the jet axis and moving in different directions to the line of sight. Their model in which the electron acceleration site was supposed to be in the jet-forming region could also explain the H.E.S.S. spectrum, but the supposition is somewhat incompatible with the latest observational result that the γ-rays are produced in the whole jet (Abdalla et al. 2020). Assuming more intense magnetic-field strength than in the conventional SSC modeling, Petropoulou et al. (2014) considered the VHE emission that stems from a hadronic component, on the basis of the single-zone SSC model. Inverse Comptonization (IC) of dust emissions by electrons accelerated at velocity shear (Liu et al. 2017; Mbarek et al. 2025) might be a process of the VHE γ-ray production, which would be compatible with the H.E.S.S. result (Abdalla et al. 2020). In any case, the substantial observations prompt us to elucidate a fundamental mechanism of particle acceleration responsible for the low-energy spectral hump from radio to X-rays being arguably reflected in the γ-ray hump.

The broad γ-ray image is reminiscent of ubiquity of X-ray knots in the jet. The high-resolution X-ray images (Kraft et al. 2002) reveal that the X-ray knots are embedded in radio knots (Burns et al. 1983, hereafter BFS83) and similar in form to them, implying the common acceleration mechanism for electrons emitting the synchrotron photons. In terms of this aspect, we conceive that the X-ray knots, which can be associated with shock waves (Kraft et al. 2002), represent a major origin of the VHE γ-ray fluxes. The shock is generated by collision of flowing plasmas and could realize the diffusive shock acceleration (DSA) of electrons and positrons in situ (Drury 1983; Biermann & Strittmatter 1987). On the other hand, the violent situation is known to be unstable for the electromagnetic current filamentation (Weibel-like) instability (e.g., Honda 2004; Kato 2007). Nonlinear development of the turbulent state results in the nonuniformity of magnetic fields (Silva et al. 2003), which should be incorporated in the modeling of the accelerator as the synchrotron emitter.

This motivated us to consider an inhomogeneous SSC process in the kiloparec-scale jet as a possible mechanism of the VHE γ-ray production. For the scale-invariant magnetized current filaments reflecting self-similarity, the magnetic-field strength depends on the transverse size, λ, of the filaments, conforming to the turbulence spectrum of $B_k^2/8\pi$, with k being $2\pi/\lambda$ (e.g., Montgomery & Liu 1979). The field strength of the thinner

⋆ Corresponding author: honda@ktc.ac.jp

filament is weaker than that of the largest filament comparable to the global mean inferred from energy equipartition with photon fields. Thus, we can expect, in accordance with foregoing the X-ray observation, that electrons in the thinner filaments be accelerated to higher energies; this is due to the suppression of synchrotoron cooling. In simple modeling with evenly fragmented multi-blobs, it is hard to postulate such a weak magnetic field without violating consistency with the global equipartition. Concerning the comparison with the spectral measurement, the point is that the brighter knots close to the nucleus are obscured by thick dust lane in the infrared to the ultraviolet band. This makes the direct comparison with their intrinsic nonthermal spectra difficult. Thus, building the SSC model accountable for the VHE fluxes is directly linked to the key problem: how to reasonably construct, in the inner jet, the synchrotron X-ray spectrum including the extended high-energy tail and its cutoff, as reconciled with the X-ray fluxes measured in the Chandra band (Kraft et al. 2002).

In this work, we adopted a phenomenological approach to constructing the radiation spectrum in the radio to the γ-ray range. Rather than solving the kinetic equation with a monoenergetic injection term to obtain temporal evolution of the electron energy distribution, we focused on the detailed internal structure of the jet, considering the steady distribution. We address the fact that the inhomogeneous SSC processes in the filamentary jet-knots are likely a major mechanism behind the VHE γ-ray production. The model is based on the DSA of electrons trapped in the magnetic field of the scale-invariant filaments, and the competition with energy loss processes is assessed quantitatively for each of the filaments. It is demonstrated that in the thinner filaments with the weaker magnetic fields, the electrons are accelerated to higher energy levels, and in the bright X-ray knots of the inner jet, the maximum Lorentz factor reaches 10^9 in a critical region where synchrotron cooling time of the electrons is comparable to the timescale of their local escape from there. In the DSA sites distributed in the kiloparsec-scale jet, the theoretical synchrotron spectra are constructed by numerically superposing the fluxes from the numerous filaments. Taking account of radiative cooling of the filaments and the SSC process in knots A and B, we reproduced the γ-ray hardening observed by the H.E.S.S. The physical parameters such as the compression ratio of the scattering center, magnetic field strength, and so on, required for spectral reproduction were fixed within a narrow range. If we consider the contribution from diffuse regions of an outer jet far away from the central engine, the data observed by the Fermi-LAT can almost be reproduced in the range of 10–100 GeV.

In Sect. 2, we provide an explanation of the filamentary jet model, in terms of its application to the knots of Cen A; that is, the self-similar structure formed by the generation and nonlinear development of the current filaments (Sect. 2.1), the DSA and energy-loss processes in the filaments (Sect. 2.2), the semi-numerical method of constructing the synchrotron spectrum (Sect. 2.3), and conceivable inverse Compton (IC) processes (Sect. 2.4). In Sect. 3, the reproduced spectra of knots and a diffuse region are shown and compared with the H.E.S.S. and Fermi fluxes. Section 4 is devoted to the conclusion and a discussion on spectral variability.

2. Theoretical modeling

2.1. Filamentary knots and the self-similarity

The jet bulk may be composed of electron-positron plasma (e.g., Hirotani et al. 2000), but it is enough for our purpose to consider

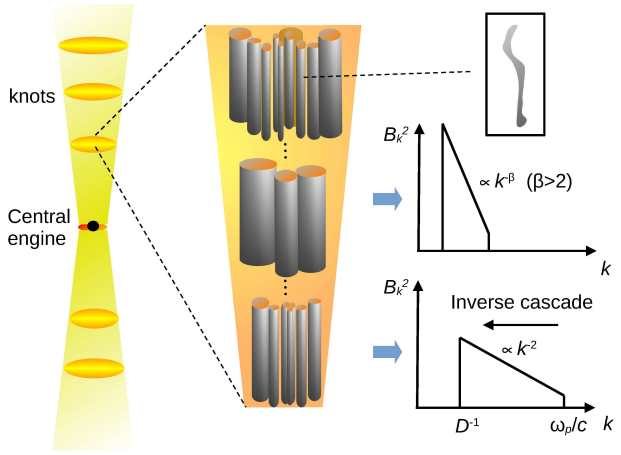

Fig. 1. Schematic view of current filamentation and coalescence in a knotty region. When plasmoids ejected intermittently from the central engine catch up with the preceding flow, the bulk breaks up into numerous separate fragments. The filaments are represented by many pipes; the inset illustrates a sample of the realistic one that is bent or twisted. The filaments soon coalesce due to the attractive force acting on the currents in the same direction. These processes actively repeat because of multiple shocks. The corresponding spectra of turbulent magnetic fields are depicted on the right side. The filamentation is driven at the scale of plasma skin depth (c/ω_p), and the magnetic-field energy accumulates on the largest scale (D) via the inverse cascade in the k space (left-pointing arrow).

the acceleration of (emissions from) electrons only, relying on the charge symmetry. The filamentation instability is expected in the jet knots or blobs (Honda & Honda 2007) and in a huge-current-carrying jet as well (Honda & Honda 2002); the former, involving shocks, is part of the present issue. In our view, each of the radio knots (such as A, B, ...) with the jet's width contains multiple shocks, as intermittent activities of the central engine lead to successive impingement of ejected plasmoids on the preceding slower ones. We envisage that inside the knot, the filamentation driven by the shocks, coalescence of the current filaments, and condensation of magnetic energy (Honda et al. 2000; Silva et al. 2003) are taking place everywhere, so the filaments are present not only behind the shocks, but also ahead of them. The power-law spectrum of the turbulent magnetic fields, $B_k^2 \propto k^{-\beta}$, effectively appears in the inertial range resulting from the inverse cascade. That is, due to the attractive force acting on the currents in the same direction, some of them coalesce each other into the larger one. The expected self-similar structure is in accordance with the observed features of subknots in a knot (Kraft et al. 2002) and subsubknots in a subknot (Hardcastle et al. 2003; Snios et al. 2019). Figure 1 schematically shows the dynamical picture of the filamentary knot as a filament's "wood". When the filamentation is actively occurring, the turbulent spectral index reflects an ideal state of two-dimensional turbulence of transverse magnetic fields as $\beta = 2$ (Montgomery & Liu 1979). In the advanced stage of turbulence, the value of β likely increases (Silva et al. 2003), but the subsequent filamentation will reset it to 2. Because of the multiplicity of the shocks, these processes repeat, to virtually equilibrate inside the knot. In knots of the outer jet, weaker shocks and/or longer intervals among the shocks may bring about a larger effective β value, if at all.

After transit of a shock train, i.e., in a post-knot region, the filamentation is no longer active, so the accumulation of larger filaments is prominent. The phase of energy condensation at the

largest scale of the jet width could be also expected in the diffuse regions of the outer jet. The situation in which small filaments are swept away, leaving only a few large filaments, is similar to the special case in which exists solely a filament, as compared to the single-zone model.

Meanwhile, the plasma will magnetohydrodynamically evolve toward an energy-relaxed state in order to self-organize the force-free helical flow (Chandrasekhar & Kendall 1957; Broderick & Loeb 2009), which is impinged upon by the leading edge of subsequent shocks. The theory suggests that in a lower luminosity region between knots, the jet may lose its sharp shear, as it has a rather smooth velocity distribution. The specific configuration likely degrades efficiency of the shear acceleration, but acts as a pre-stage accelerator to inject seed electrons into the forthcoming shocks.

2.2. Diffusive shock accelerator of electrons

Locally ordered magnetic fields of the filaments are inevitably disturbed by the Alfvén waves. We assumed that the energy-density ratio (denoted as b), of the fluctuating magnetic fields to the mean field $B(\lambda;\beta)$, is constant smaller than unity and independent of λ. The gyrating electrons bound to the mean field of a filament are resonantly scattered when the condition $r_g \sim k'^{-1}$ is satisfied (Drury 1983), where $r_g(\gamma_e, B)$ and $k'(\geq k)$ are the gyro-radius of the electron with the Lorentz factor, γ_e, and wave number of the Alfvénic fluctuations, respectively. The successive small-angle deflections enable the electrons to go back and forth across the shock statistically; this is a subject of the Fermi-based DSA mechanism. In the plasma configuration argued in Sect. 2.1, the magnetic-field lines tend to be largely inclined, rather than parallel, with respect to the shock-normal direction. Besides this, the inclination angle is distributed when the filaments are wiggling (see Fig. 1 inset), as seen in observations (Giovannini et al. 2018; Fuentes et al. 2023; Raiteri et al. 2024). In this respect, an average of the inclination angle upstream of the shock was considered, and its value was set to the de Hoffmann-Teller limit: $\theta = \cos^{-1}(U/c)$ (with the shock speed of $U = 0.5c$ comparable to the speed of proper motion: Hardcastle et al. 2003), in which the acceleration efficiency is at its maximum (Honda & Honda 2005). Taking all this into account, the characteristic acceleration time of the electron is given by $t_{\rm acc} = [3\eta r/(r-1)](r_g/c)$, where r is the scattering center compression ratio, which is precisely related to the gas compression ratio (Schlickeiser 2002), and

$$\eta = \frac{3}{2b}\left(\frac{\lambda}{2r_g}\right)^{\frac{2}{3}}\left[1+\frac{r}{(\cos^2\theta + r^2\sin^2\theta)^{3/2}}\right], \quad (1)$$

which is valid when k' is of the inertial range of the Kolmogorov spectrum (Biermann & Strittmatter 1987).

With regard to the processes that limit the acceleration, it is crucial for the temporal limit to take synchrotron radiation loss into account, provided that the energy density of the magnetic field, $u_{\rm m} = B^2/8\pi$, is locally comparable to that of synchrotron photons $u_{\rm ph}$, or more. The extended argument on photon fields is given later in Sect. 2.4. We did not take account of an adiabatic expansion effect of the acceleration regions, since the magnetic self-collimation (Honda & Honda 2002) will significantly prevent them from expanding at least radially outward. Then, for the electrons bound to stronger magnetic fields of larger filaments, the acceleration is limited by the synchrotron cooling time of $t_{\rm syn} = 3m_e c/4\sigma_{\rm T}u_{\rm m}\gamma_e$, where $\sigma_{\rm T}$ is the cross-section of Thomson scattering, and the other notations are standard. The equation of $t_{\rm acc} = t_{\rm syn}$ provides the solution for γ_e, namely, the maximum Lorentz factor (denoted as γ^*) determined by the temporal limit. On the contrary, for the electrons in smaller filaments, the escape loss overcomes the synchrotron loss; note here that "escape" does not mean running away from the jet width. In other words, the spatial limit $r_g = \lambda/2$ determines γ^* in that regime. It is remarked that the local escape could successively occur until the electrons are trapped in a filament larger than $\lambda_{\rm c}$, to be further energized or radiatively cooled. The critical size of the filament $\lambda_{\rm c}$ exists, at which point the energy restriction of electrons switches from the temporal to the spatial limit (Honda & Honda 2007). The achievable maximum of γ^* is realized at $\lambda_{\rm c}$, to give the synchrotoron cutoff frequency. We numerically evaluated γ^* for various filament sizes, λ, based on which we constructed the synchrotron spectrum via the method explained below.

2.3. Semi-numerical method of constructing theoretical synchrotron spectra

The theoretical maximum value of λ is limited by the observed transverse size of the knots and the diffuse region, both of which are denoted as D_j. Here, the maximum of λ, denoted as D, is given by $f_{\rm cr}D_j$, where $f_{\rm cr}$ is a parameter less than unity, which stands for correlation reduction of the filamentary turbulence. On the other hand, a theoretical minimum of λ is limited by the plasma skin depth of $c/\omega_p \sim 5\times10^5 n_e^{-1/2}$ cm (see Fig. 1), where ω_p and n_e (in cm^{-3}) are the angular frequency of plasma oscillation and number density of electrons (typically, $n_e \sim 10^{-2}$ cm^{-3}; BFS83), respectively. Between D and c/ω_p, the scale of λ is supposed over many orders of magnitude, as compared to the powers of the tenth structure of radio jets (Bridle & Perley 1984). The related self-similar feature is illustrated in Fig. 2, along with the relation between D and D_j. In the modeling, were we introduce the effective minimum $d(\geq c/\omega_p)$, we obtain $D/d = 10^n$, with n being allowable up to ~15.

The contribution of various filaments to the flux is considered as follows. In the λ space, numerical filaments with the total number, N, are distributed at equal intervals, $\Delta = n/N$, on an exponent with no characteristic length scale. Let S_i be the area of cutting edge of the i-th filament and $\mathcal{F}(S_i)$ be the size distribution of the filaments. As the specific form of $\mathcal{F}$ is unknown, we assume that it has a form such as $\mathcal{F}(S_i) = (S_i/S_0)^{-q}$, where q is a constant satisfying $0 \leq q < 2$. Then, we have the following requirement:

$$\sum_{i=0}^{N}\mathcal{F}(S_i)S_i = \frac{S_0\{1-[10^{-(2-q)\Delta}]^{N+1}\}}{1-10^{-(2-q)\Delta}} = \frac{\pi}{4}f_p D_j^2, \quad (2)$$

where $S_0 = (\pi/4)D^2$, with $D = f_{\rm cr}D_j$ being the area of the largest filament and f_p the filling rate of filaments in the jet, which satisfies $f_{\rm cr}^2 < f_p < 1$. From Eq. (2) for $N \gg 1$, we have $f_{\rm cr}^2/f_p = 1 - 10^{-(2-q)\Delta}$, which is written as $(2-q)n = -N\log_{10}(1-f_{\rm cr}^2/f_p) > 0$. In the calculation of the DSA and construction of synchrotron spectrum, the parameter f_p is merely involved in the logarithmic argument, whereas varying the value of $f_{\rm cr}$ directly affects the shape of the spectrum (the break frequency appears proportional to $f_{\rm cr}^{-1}$; cf. Eq. (3)). For simplicity, therefore, we set the filling rate as $f_p = 0.5$. Then, regarding the unknown quantity of $(2-q)n$ as invariant of the turbulent dynamics, we changed N when varying the $f_{\rm cr}$ value in spectral fitting.

As for the electron acceleration, the DSA mechanism generates the energy distribution of electron density $n(E)dE \propto E^{-p}dE$

with $p = (r+2)/(r-1)$, where p is assumed to be constant in each of the emission regions. Note here that p is not decomposed into multi-values; the steady electron distribution is presumed to happen as a continuous injection, instead of via solving the kinetic evolution. We considered synchrotron emissions from the electrons in the i-th numerical filament to measure λ_i, and then we summed them all. The relativistic beaming effect was ignored (Abdalla et al. 2020). Provided $n(E) = c_i E^{-p}$, with c_i being a constant for the i-th filament, the number density of electrons injected into the i-th filament is given by $n_i \simeq [c_i/(p-1)]E_{\mathrm{min},i}^{-(p-1)}$, where $E_{\mathrm{min},i}$ is the energy of the injected electrons. The emissivity per unit volume of the i-th filament can be approximately expressed as $J_i(\nu) \approx c_i B(\lambda_i)^{\frac{p+1}{2}} \nu^{-\frac{p-1}{2}} \exp(-\nu/\nu_i)$ (e.g., Longair 1994), where $B(\lambda_i) = B_{\mathrm{m}}(\lambda_i/D)^{(\beta-1)/2}$ with $B_{\mathrm{m}} = B(\lambda_0 = D)$, and $\nu_i = (3/4\pi)e\gamma_i^2 B(\lambda_i)/m_e c$ with $\gamma_i = \gamma^*(\lambda_i)$. Here, a factor on the order of unity (dependent on p, etc.) has been ignored. To evaluate the luminosity, $L_{\nu,i}$, of the i-th filament, the $J_i(\nu)$ must be multiplied by the area of the filament S_i and the number of filaments of that size: $\mathcal{F}(S_i) = \mathcal{F}_i$. That is, we have $L_{\nu,i} \approx \kappa_i B(\lambda_i)^{\frac{p+1}{2}} \nu^{-\frac{p-1}{2}} \exp(-\nu/\nu_i)$, where the i-dependent coefficient is explicitly given by $\kappa_i = c_i \mathcal{F}_i S_i = n_i(p-1)E_{\mathrm{min},i}^{(p-1)} \mathcal{F}_i S_i$. For the likely $p \simeq 2$ that corresponds to $r \simeq 4$, we have $\kappa_i \simeq \mathcal{F}_i S_i n_i E_{\mathrm{min},i}$, and therefore, κ_i can be claimed to almost stand for the total energy of electrons injected into the i-th-sized filaments. In any case, the sum $\sum_{i=0}^{N} L_{\nu,i}$ provides, in effect, the quantity that could be compared with the observed flux density, F_ν, of the emission region. Were we assume $\kappa_i \sim$ const. $= \kappa$, the summation is significantly simplified; for example, both the cases of $\kappa = S_i n_i E_{\mathrm{min},i}$ for given $(q,n) = (0,\mathfrak{n})$ and $\kappa = S_0 n_i E_{\mathrm{min},i}$ for $(q,n) = (1,2\mathfrak{n})$ apparently lead to the same F_ν while allowing the different interpretation of the actual turbulent state of filaments and injection conditions. At this juncture, we demonstrate the specific calculation with such an invariant κ and $(q,n) = (0,6)$ ($\leftrightarrow (1/3, 7.2)$, $(1/2, 8)$, etc.; the related coverage of λ is verified below). Indeed, the setting that tacitly allows for $n_i E_{\mathrm{min},i} \propto 1/S_i^{1-q}$ with $q < 1$ is physically relevant in that the electron density is expected to be higher in the radially inner region of jet, where the electron energy is higher according to the X-ray observation, suggesting that a large amount of energetic particles are confined in a narrower channel of the inner region (Kraft et al. 2002).

Figure 3 shows, for example in knot A, the calculated γ^* of electrons trapped and accelerated in the filaments of the various sizes (top) and the flux of synchrotron radiation from the electrons in some representative filaments (bottom). In the top panel, one can see that when the filament size, λ, is larger than the critical size, λ_{c}, γ^* is determined by the temporal limit due to the synchrotron cooling, while $\lambda < \lambda_{\mathrm{c}}$, γ^* is determined by the spatial limit, as discussed in Sect. 2.2. The filaments a-d labeled in the upper and lower panels correspond to each other. At the largest filament, a, the radio-optical flux is of the highest level owing to $B = B_{\mathrm{m}}$, while γ^* is low. The cooling time, $t_{\mathrm{syn}} \simeq 1.2 \times 10^8$ s, is much shorter than the timescale of the escape from this filament, i.e., on the order of 10^{10} s. As for the thinner filament, b, the flux decreases due to $B < B_{\mathrm{m}}$, and γ^* increases. At the even thinner filament, c, with $\lambda_{\mathrm{c}} = 0.16$ pc, the flux drops further, whereas γ^* and the corresponding synchrotron frequency reach their maximum; $t_{\mathrm{syn}} \simeq 5.7 \times 10^8$ s is comparable to the escape time. At filament d, where λ and B are still smaller, the escape from the filament dominates the synchrotron loss, and, correspondingly, both γ^* and the synchrotron frequency decrease (thin dotted curve in the bottom). This figure also clarifies that synchrotron radiation from electrons in the thin filament of $\lambda \ll \lambda_{\mathrm{c}}$ contributes very little to the 'Total' spectrum, indicating that the coverage of λ presumed above is reasonable. As a result, the radiation from the largest filament, a, appears to form the break in the spectrum, while that from filament c forms the cutoff of the spectrum. The synchrotron break and cutoff frequencies are defined by $\nu_{\mathrm{b}} = \nu_0(\gamma_0, B_{\mathrm{m}})$ and $\nu_{\mathrm{c}} = \nu(\gamma_{\mathrm{c}}, B(\lambda = \lambda_{\mathrm{c}}))$, respectively, where $\gamma_0 = \gamma^*(\lambda_0)$ is denoted as γ_{b} and $\gamma_{\mathrm{c}} = \gamma^*(\lambda = \lambda_{\mathrm{c}})$.

Cooling after the acceleration, i.e., the aging effect of electrons, may be important for modeling a lower activity region similar to the hot spots of Fanaroff-Riley class II (FR-II) radio galaxy lobes (e.g., Meisenheimer et al. 1997; Brunetti et al. 2003; Cheung et al. 2005). The effect is, however, reasoned to be ignorable for the FR-I jet-knot environments, where the violent intermittent activities constantly take place such that a trail of working regions of the DSA successively captures electrons being radially confined by relatively ordered magnetic fields.

2.4. Inverse Comptonization

For the major IC, we considered the local SSC. That is, the photon frequency boosted via the IC, $\nu_{\mathrm{ic}} = \gamma_e^2 \nu$, which is proportional to $\nu^2/B(\lambda_i)$, was calculated for each filament; the corresponding photon fluxes from all filaments were summed up. Concerning u_{ph} as the target photon fields, $\langle u_{\mathrm{ph}} \rangle \lesssim \langle u_{\mathrm{m}} \rangle$ was inferred from an approximate equipartition relation inspected in an inner jet region closer to the nucleus for the global mean over the concerned emission region (Meisenheimer et al. 2007); there, the emission region better matches the electron acceleration region. In addition, in the situation in which filaments sparsely distribute (see Fig. 2), it is thought that the effect of radiative transfer is more pronounced in thinner filaments, causing larger deviations from the equipartition relation locally. Indeed, if all the low-energy photons are ideally boosted up to higher energies by the IC, the evaluated flux of the high-energy photons $(\nu F_\nu)_{\mathrm{ic}}$ exceeds the observed level. In this respect, we took into account the effect that prevents the ideal boosting of all photons. First, the relation $u_{\mathrm{ph}}/u_{\mathrm{m}} \lesssim 1$ is expected to decrease $(\nu F_\nu)_{\mathrm{ic}}$ below the synchrotron νF_ν level. Second, for the thinner filaments, the larger emitting surface-to-volume ratio will increase the radiative cooling of filaments significantly; this includes the radiator effect. For a one-dimensional approximation of a fragmented column, we employed the model that $u_{\mathrm{ph}}/u_{\mathrm{m}}$ decreases by the factor λ/D, instead of solving the details of the radiative transfer. This would reflect the ratio of the scale λ of filaments to a typical mean free path of synchrotron photons (close to the free-streaming limit, in certain cases). Besides, the filament suffers synchrotron photons emanating from the other filaments. Yet, even if the energy loss of the photons during the inter-filament transport is negligible, the influence of larger filaments on smaller ones is limited to the IC of the lower energy photons (see Fig. 3, bottom panel); the influence of the smaller one on the larger one will be negligible. As it stands, the nonlocal SSC due to this effect is thought of as being less dominant, compared with the local one. Accordingly, combining the two, we have $u_{\mathrm{ph}}/u_{\mathrm{m}} = a(\lambda/D)$ with $a \lesssim 1$, which is reflected in $(\nu F_\nu)_{\mathrm{ic}}/(\nu F_\nu)_{\mathrm{syn}}$, involving the implication of $a \sim f_{\mathrm{cr}}$ (see Table 1). It is noted that the model with $a < 1$, substantiated below, ensures the maximum energy analysis in which $t_{\mathrm{acc}} = t_{\mathrm{syn}}$ is solved for the electron DSA. The Klein-Nishina effect is also included. Superposing the spectra that involve these effects, we obtain the boosted nonthermal spectrum, which could be compared with the observed γ-ray fluxes.

We mention, in addition to the synchrotron component, another potential candidate for target photons; i.e., the so-called external component: the contribution from the other parts of

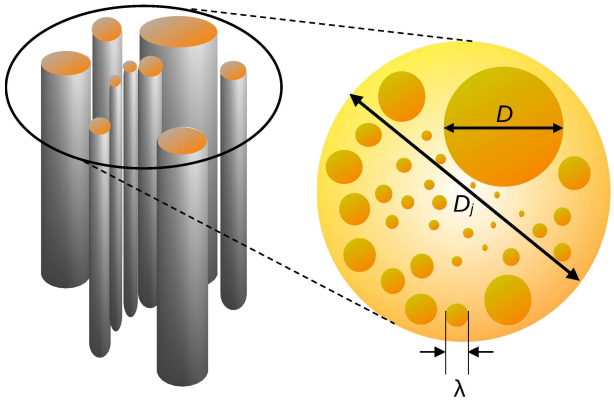

Fig. 2. Transverse cut of knotty region that contains, with a filling rate less than unity, filaments with various transverse sizes, λ. Note the relation of $\lambda \leq D < D_j$, where D is diameter of the largest filament and D_j corresponds to diameter of the jet.

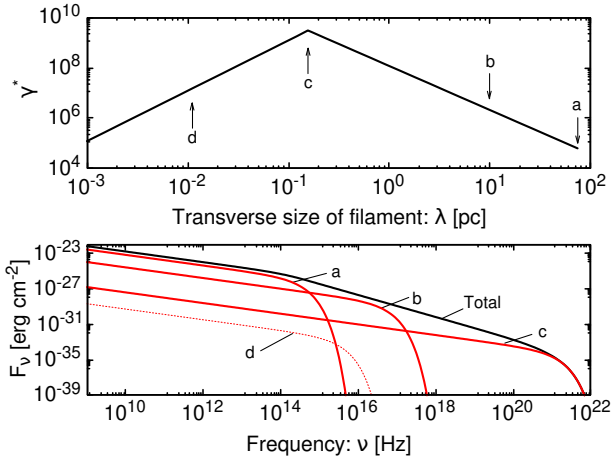

Fig. 3. Maximum Lorentz factor of electrons accelerated in the filaments with various sizes, λ, in a knot (top) and flux density due to contribution from sampled filaments (the labels a-d correspond to these; bottom panel). The solid black curve (labeled Total) shows the flux that is the sum of contributions from all filaments in the considered λ range. For an explanation, see the text.

Cen A. Considering the entire system, various regions are possible, such as the central engine, circumnuclear disk, thick dust lane, and so on. Of particular interest to us is the region that may affect γ-ray hardening, and hence we focused on the nucleus with radiation contributions in the visible light and higher energy regions. The active nucleus was investigated by Marconi et al. (2000) with Wide Field and Planetary Camera 2 (WFPC2) and Near Infrared Camera and Multi-Object Spectrograph (NICMOS) observations of the Hubble Space Telescope (HST). They explain the optical and near-infrared emission by the combination of the nonthermal power law extrapolated from X-rays reddened by 14 mag and modified blackbody emission at 700 K probably caused by emission from hot dust within 2 pc of the nucleus. Alternatively, interferometric observations with Mid-infrared Interferometric Instrument (MIDI) revealed the existence of a well-resolved disk and an unresolved core in the innermost parsec of Cen A (Meisenheimer et al. 2007). Using their results combined with the earlier data (Marconi et al. 2000), they demonstrated that the core spectrum can be approximated by the power-law synchrotron spectrum of $F_\nu \propto \nu^{-0.36}$ that was cut off exponentially above the frequency of $\nu \sim 8 \times 10^{13}$ Hz; the core is optically thick below ~45 GHz. A thermal component of a geometrically thin disk whose diameter is about 0.6 pc containing dust heated up ~240 K also contributes between 20% (at the radio wavelength of 8 μm) and 40% (at 13 μm) to the nuclear flux. Even if the photons from the nuclear region could reach knot A or B without significant energy loss, the Lorentz factor of the major electrons that would upscatter them would be on the order of $\gamma_e \sim 10^4$–10^5 (see Fig. 3, panel top). Therefore, the frequency of boosted photons would be at most $\nu_{\rm ic} = \gamma_e^2 \nu_{\rm syn} \sim 10^{21}$–$10^{22}$ Hz, which is far below the H.E.S.S. band. The contribution of external components to the spectrum of the diffuse region is discussed later in the paper.

3. Results: Reproduction of the observed γ-ray fluxes

We applied the filament model discussed in Sect. 2.1 to knots A and B including many nested subknots and subsubknots, and determined the physical parameters required for the spectral evaluation. In addition to the key parameter $B_{\rm m}$, the free dimensionless parameters of the model are r, b, β, $f_{\rm cr}$, and a, whose domains are $1 < r \leq 4$, $b \ll 1$, $\beta \geq 2$, $f_{\rm cr} < 1$, and $a \lesssim 1$, respectively. For the knots, it might seem difficult to fix the physical parameters because of the lack of flux data in the infrared to the ultraviolet band (Sect. 1). However, we see that the values can be determined within a narrow permissible parameter window with reference to synchrotron flux data in the outer diffuse regions (Hardcastle et al. 2006) and γ-ray data (Abdalla et al. 2018).

In particular, the value of $B_{\rm m}$ is tightly restricted by the pivotal relation $\nu_{\rm ic,b} = 2.4 \times 10^{23} (10\ {\rm mG}/B_{\rm m})(\nu_{\rm b}/10^{14}\ {\rm Hz})^2$, where $\nu_{\rm ic,b}$ is the frequency at which the $(\nu F_\nu)_{\rm ic}$ spectrum breaks to take the peak value. That is, we obtain $B_{\rm m} \sim 10$ mG from combining the expected $\nu_{\rm ic,b} \gtrsim 10^{23}$ Hz and $\nu_{\rm b} \sim 10^{14}$ Hz comparable to that observed in the outer diffuse regions. Regarding the shock strength, we supposed the situation in which the multiple shocks are not superposed, but spatially distributed, so that the compression ratio did not exceed the strong limit. Meanwhile, it is natural to consider that the shocks are weakened as they propagate outward; in the diffuse regions, radio-infrared data (Hardcastle et al. 2006) suggest $r \leq 3.3$. Accordingly, for the knots closer to the nucleus, the expected r range reduces to $3.3 \leq r \leq 4$. For a given D_j, and the constraints on $B_{\rm m}$ and r, we can estimate the value of b from

$$b \simeq 0.055 \frac{r}{r-1} f(r,\theta) \left(\frac{\nu_{\rm b}}{10^{14}\ {\rm Hz}}\right)^{\frac{2}{3}} \left(\frac{D}{100\ {\rm pc}}\right)^{\frac{2}{3}} \left(\frac{B_{\rm m}}{10\ {\rm mG}}\right), \qquad (3)$$

where $f(r,\theta)$ is the factor $[1 + \cdots]$ given in Eq. (1). Provided the $\nu_{\rm b} \sim 10^{14}$ Hz and the plausible range of $f_{\rm cr} \gtrsim 10^{-1}$, we have $b \sim 10^{-1}$; i.e., virtually the maximum. Concerning β, it is unlikely that the effective value deviates significantly from two (see Sect. 2.1). Its combination with the r value determines the X-ray spectral index. Following this, the specific shape of the γ-ray spectrum was determined; the flux level was then adjusted by the coefficient, a, of the cooling factor. Assuming that absorption of the γ-rays by diffuse extragalactic background light is negligible (Aharonian 2004), the theoretical spectrum was constructed as a better fit to the fluxes measured in multiple bands over radio-to-VHE γ-rays.

The parameter values we used here are summarized in Table 1, along with the observed D_j of the major knots and the diffuse region. For knots A and B, the synchrotron spectra are

Table 1. Physical properties of major knots and diffuse region.

Name[a]	D_j[b] (pc)	B_m (G)	r	b	β	f_{cr}	a
knot A	147.9	0.01	3.5	0.1	3	0.5	0.4
knot B	173.4	0.01	3.4	0.2	3	0.5	0.4
Diffuse	714	0.01	3.3	0.3	–	0.1	0.4

Notes. [(a)]Name of the X-ray-emitting regions that contain smaller X-ray (sub/subsub)knots. The diffuse region corresponds to the rectangular "Inner" region defined in Hardcastle et al. (2006). [(b)]The jet width at each region (for the knots, radio-20 cm: BFS83).

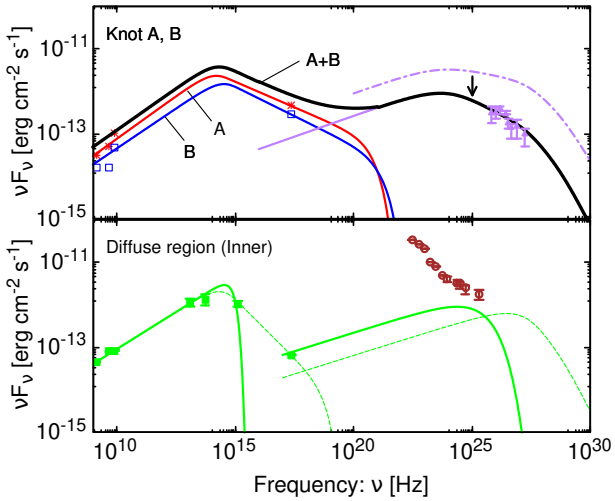

Fig. 4. νF_ν spectra of the knots (top) and diffuse region (bottom) in the radio-to-γ-ray range for the parameter values given in Table 1. For the knots, the observed radio fluxes are cited from BFS83, and the X-ray fluxes are obtained by adding up the fluxes of subknots (Kraft et al. 2002). The calculated spectra and observed fluxes of knots A and B are denoted by the red and blue curves and marks (asterisks; open-squares), respectively. The solid and dot-dashed purple curves show the calculated spectra of the IC component (knots A+B) with and without radiative cooling effect of filaments, respectively. The overall spectrum of synchrotron+IC is shown as a solid black curve. The calculated spectra of the diffuse region are denoted by green curves, and the observed fluxes from that region (green crosses) are cited from Hardcastle et al. (2006). The cases for which the observed X-ray flux is assumed to originate from synchrotron radiation and IC (+radiative cooling) are, respectively, shown by the thin dashed and bold curves. The observed γ-ray fluxes of the H.E.S.S. (top: purple triangles) and Fermi-LAT (bottom: brown open-circles) are cited from Abdalla et al. (2018).

shown in Fig. 4 (top) via red and blue curves, respectively; the former corresponds to "Total" in Fig. 3 (bottom). For knot A and B, the X-ray F_ν spectral indices are estimated as 1.2 and 1.3, respectively, and Lorentz factors of the electrons making the major contribution to the spectra at, for example, 1.4 keV are $\gamma_e = 1.3 \times 10^7$ and 1.1×10^7, which are generated in the size of $\lambda = 3.5$ pc and 5.8 pc where $B = 0.48$ mG and 0.67 mG, respectively. For convenience, the resulting values of γ_b, γ_c, ν_b, and ν_c are listed in Table 2 (for knot A, compare with Fig. 3). The $\gamma_c \sim 10^9$ provides the theoretical upper limit of the electron Lorentz factor, which amenable to the argument in Abdalla et al. (2020). We find that ν_c reaches mega-electronvolt γ-ray band and the spectra extended above ν_b in the bright knots make dominant contributions to establishing the observed γ-ray hardening. In the top panel, the theoretical $(\nu F_\nu)_{ic}$ spectra including the Klein-Nishina (KN) effect and the KN plus radiator effects are

Table 2. Break and cutoff frequencies and the corresponding Lorentz factor of electrons.

Name	γ_b	γ_c	ν_b (Hz)	ν_c (Hz)
knot A	6.3×10^4	3.0×10^9	1.7×10^{14}	8.2×10^{20}
knot B	9.7×10^4	4.0×10^9	3.9×10^{14}	1.6×10^{21}
Inner	–	1.4×10^5	–	8.5×10^{14}

denoted by dot-dashed and solid curves, respectively. The spectral depression by the radiative cooling is indicated by the arrow and is found to be noticeable in the VHE range and above. The overall multiwavelength spectrum of the combined synchrotron and IC components is also shown by the thick black solid curve.

Some lower luminosity X-ray features (e.g., FX1, ..., GX1, ...; Snios et al. 2019) that have recently been resolved in the outer diffuse regions ("Inner" and "Middle"; Hardcastle et al. 2006) appear to be similar to the well-known X-ray subknots (AX1, ..., BX1, ...: Kraft et al. 2002) in the knots (A and B; BFS83). This potentially allows us to apply the current method to the diffuse regions in a common way, except for differences in the physical parameters. In Fig. 4 (bottom), for the parameters of the diffuse region given in Table 1 with $\beta = 6$, we show the spectrum of synchrotron radiation from the "Inner" region and its upscattered spectrum via the IC with dashed green curves. We see that interpreting the observed X-ray flux as the synchrotron origin fails to reproduce the γ-ray data, as far as the SSC is presumed. It does not mean, however, that the filament model itself is ruled out there. If coupling this model with the external Comptonization of dust emissions (from the nuclear disk or dust lane as mentioned above), one might account for the observed γ-ray spectrum up to the VHE range. However, here we consider an alternative possibility: the case in which filamentation has already ceased, and the coalescence of filaments has proceeded, leaving a single large filament in accordance with the discussion in Sect. 2.1. This just corresponds to the single-zone modeling; for the same parameter set (but, now free from β), we show the spectrum in the same panel (bottom) via a thick solid green curve. For this case, the values of $\gamma_c(=\gamma_b)$ and $\nu_c(=\nu_b)$ are listed in Table 2. Although the solo contribution from the "Inner" part of the diffuse region is not quite enough to account for the observed Fermi fluxes, it is anticipated that the observed ones can be explained by adding the contributions from the knots and/or the other diffuse regions.

4. Concluding remarks

In conclusion, we find that the major origin of the spectral hardening of the VHE γ-ray fluxes in Cen A could be ascribed to the inhomogeneous SSC in the bright X-ray knots distributed in the jet; synchrotron loss of the DSA is markedly suppressed for the electrons trapped in the weak magnetic field of thin filaments. In particular, the model reflects the common self-similar structure and turbulent evolution of the internal jet, and, as it is, it provides a promising alternative to the external Compton (Tanada et al. 2019) and shear acceleration (Liu et al. 2017) scenarios. In our concept, once the filament parameters, which are somewhat constrained by independent observations, are fixed, the key factors characterizing the spectral shape (e.g., the break and cutoff frequencies, the power-law exponent, etc.) are derived. Unlike conventional single-zone SSC models, it is no longer necessary to explicitly specify the maximum and minimum values of the

electron Lorentz factor or the second exponent of the broken power-law spectrum.

This paper does not deal with the steep rise in νF_ν flux observed by the TANAMI Very Long Baseline Interferometry (VLBI; for the archival data: Abdo et al. 2010) and HST (Marconi et al. 2000), which is deemed to be the thermal and/or nonthermal component ranging from radio-to-infrared wavelengths. The narrow high-energy peak between the X-rays and soft γ-rays observed by SUZAKU (Markowitz et al. 2007) and Swift-Burst Alert Telescope (BAT; Ajello et al. 2008), respectively (not shown in the figure), which is thought to comprise the upscattered thermal photons (or the synchrotron photons; Lenain et al. 2008), is also beyond the scope of this study.

As for the spectral variability of Cen A, the stable nature of the X-ray spectrum was first revealed by Rossi X-ray Timing Explorer (RXTE) observations (Rothschild et al. 2011). On the other hand, Tachibana et al. (2016) reported a soft lag in the X-ray band on a timescale of days, owing to detailed analysis of the light curves measured by the Gas Slit Camera (GSC) aboard the Monitor of All-sky X-ray Image (MAXI). Although the mechanism that generated the soft lag is still unknown, the results are negative for a single-zone jet, which is incorporated in an SSC model. According to our model, the soft lag can be explained by the stronger turbulent state in an innermost region (compared to compact blazars), which reduces the β value to ∼2 or lower (Honda 2008). Our SSC model can also respond to the variability of γ-rays and that of synchrotron X-rays; i.e., the γ-ray variability timescale can be estimated as $\tau \sim t_{\rm acc} = t_{\rm syn} \propto \lambda^{-(3\beta-7)/8}$, with λ being the solution of $\nu_\gamma = \gamma_e^2 \nu(\gamma_e, B)$ for given γ-ray energy $h\nu_\gamma = E$. Note that for $\beta > 7/3$, hard lag appears. At $E = 20\,\mathrm{GeV}$ (100 TeV), the Cherenkov Telescope Array (CTA; Biteau et al. 2020) covers the range; there, we read $\tau \sim 4.2\,\mathrm{yr}$ (6.0 yr) for the knot-A parameters, for example, along with the hard-lag appearance above one giga-electron volt. We hope that the filament model, and its applicability to the other jets, can be verified by high-spatiotemporal-resolution, multiwavelength observations including the CTA in the future.

References

Abdalla, H., Abramowski, A., Aharonian, F., et al. 2018, A&A, 619, A71
Abdalla, H., Adam, R., Aharonian, F., et al. 2020, Nature, 582, 356
Abdo, A. A., Ackermann, M., Ajello, M., et al. 2010, ApJ, 719, 1433
Aharonian, F. A. 2004, Very High Energy Cosmic Gamma Radiation: A Crucial Window on the Extreme Universe, 1st edn. (World Scientific Publishing)
Aharonian, F., Akhperjanian, A. G., Anton, G., et al. 2009, ApJ, 695, L40
Ajello, M., Rau, A., Greiner, J., et al. 2008, ApJ, 673, 96
Biermann, P. L., & Strittmatter, P. A. 1987, ApJ, 322, 643
Biteau, J., Prandini, E., Costamante, L., et al. 2020, Nat. Astron., 4, 124
Bridle, A. H., & Perley, R. A. 1984, ARA&A, 22, 319
Broderick, A. E., & Loeb, A. 2009, ApJ, 703, L104
Brunetti, G., Mack, K. H., Prieto, M. A., & Varano, S. 2003, MNRAS, 345, L40
Burns, J. O., Feigelson, E. D., & Schreier, E. J. 1983, ApJ, 273, 128
Chandrasekhar, S., & Kendall, P. C. 1957, ApJ, 126, 457
Cheung, C. C., Wardle, J. F. C., & Chen, T. 2005, ApJ, 628, 104
Chiaberge, M., Capetti, A., & Celotti, A. 2001, MNRAS, 324, L33
Drury, L. O. 1983, Rep. Prog. Phys., 46, 973
Fuentes, A., Gómez, J. L., Martí, J. M., et al. 2023, Nat. Astron., 7, 1359
Giovannini, G., Savolainen, T., Orienti, M., et al. 2018, Nat. Astron., 2, 472
Hardcastle, M. J., Worrall, D. M., Kraft, R. P., et al. 2003, ApJ, 593, 169
Hardcastle, M. J., Kraft, R. P., & Worrall, D. M. 2006, MNRAS, 368, L15
Harris, G. L. H., Rejkuba, M., & Harris, W. E. 2010, PASA, 27, 457
Hirotani, K., Iguchi, S., Kimura, M., & Wajima, K. 2000, ApJ, 545, 100
Honda, M. 2004, Phys. Rev. E, 69, 016401
Honda, M. 2008, ApJ, 675, L61
Honda, M., & Honda, Y. S. 2002, ApJ, 569, L39
Honda, Y. S., & Honda, M. 2005, MNRAS, 362, 833
Honda, M., & Honda, Y. S. 2007, ApJ, 654, 885
Honda, M., Meyer-ter-Vehn, J., & Pukhov, A. 2000, Phys. Plasmas, 7, 1302
Kato, T. N. 2007, ApJ, 668, 974
Kraft, R. P., Forman, W. R., Jones, C., et al. 2002, ApJ, 569, 54
Lenain, J. P., Boisson, C., Sol, H., & Katarzyński, K. 2008, A&A, 478, 111
Liu, R.-Y., Rieger, F. M., & Aharonian, F. A. 2017, ApJ, 842, 39
Longair, M. S. 1994, High Energy Astrophysics: Stars, the Galaxy and the interstellar mdeium, 2nd edn. (Cambridge University Press)
Marconi, A., Schreier, E. J., Koekemoer, A., et al. 2000, ApJ, 528, 276
Markowitz, A., Takahashi, T., Watanabe, S., et al. 2007, ApJ, 665, 209
Mbarek, R., Caprioli, D., & Murase, K. 2025, Phys. Rev. D, 111, 023024
Meisenheimer, K., Yates, M. G., & Roeser, H. J. 1997, A&A, 325, 57
Meisenheimer, K., Tristram, K. R. W., Jaffe, W., et al. 2007, A&A, 471, 453
Montgomery, D., & Liu, C. S. 1979, Phys. Fluids, 22, 866
Petropoulou, M., Lefa, E., Dimitrakoudis, S., & Mastichiadis, A. 2014, A&A, 562, A12
Raiteri, C. M., Villata, M., Carnerero, M. I., et al. 2024, A&A, 692, A48
Rothschild, R. E., Markowitz, A., Rivers, E., et al. 2011, ApJ, 733, 23
Schlickeiser, R. 2002, Cosmic Ray Astrophysics, 1st edn. (Springer: Berlin)
Silva, L. O., Fonseca, R. A., Tonge, J. W., et al. 2003, ApJ, 596, L121
Snios, B., Wykes, S., Nulsen, P. E. J., et al. 2019, ApJ, 871, 248
Steinle, H., Bennett, K., Bloemen, H., et al. 1998, A&A, 330, 97
Tachibana, Y., Kawamuro, T., Ueda, Y., et al. 2016, PASJ, 68, S25
Tanada, K., Kataoka, J., & Inoue, Y. 2019, ApJ, 878, 139